

Wave generation via oscillatory reconnection at a three-dimensional magnetic null point

LUIZ A. C. A. SCHIAVO ,¹ GERT J. J. BOTHA ,¹ AND JAMES A. McLAUGHLIN ¹

¹*Northumbria University, Newcastle upon Tyne, NE1 8ST, UK*

ABSTRACT

This work conducts a three-dimensional (3D), nonlinear magnetohydrodynamic (MHD) simulation to investigate wave generating, time-dependent reconnection around a magnetic null point. A non-periodic perturbation (in the xz -plane) triggers oscillatory reconnection (OR) at the 3D null, resulting in a self-sustained oscillation with a constant period P . We investigate the response of the system using three distinct wave proxies (compressible parallel, compressible transverse and incompressible parallel) as well as Spectral Proper Orthogonal Decomposition for decoupling and analyzing the resultant MHD wave behavior. We find that OR generates a slow magnetoacoustic wave of period P that propagates outwards in all directions along the spine and fan plane of the 3D null point. We also find the generation of a propagating Alfvén wave of period P , exclusively along the y -axis in the fan plane, i.e. in the direction perpendicular to the spine motion. These findings provide new insights into waves generated from a 3D null point and their implications for coronal seismology.

Keywords: Alfvén waves (23) – Solar magnetic reconnection(1504) – Solar physics(1476) – Solar coronal transients(312) – Solar coronal heating(1989) – Magnetohydrodynamics(1964)

1. INTRODUCTION

Magnetic reconnection is a key mechanism responsible for converting magnetic energy into other forms such as thermal and kinetic energy, while simultaneously driving particle acceleration and modifying magnetic topology (Pontin & Priest 2022; Browning et al. 2024). This process underlies many solar phenomena, including coronal mass ejections (Webb & Howard 2012) and the energy release associated with solar flares (Benz 2017). At smaller scales, observations of chromospheric anemone jets provide evidence that local reconnection events in the lower solar atmosphere play a role in heating the chromosphere and corona (Shibata et al. 2007). Magnetic null points are omnipresent from the photosphere to the upper corona (Régnier et al. 2008) and function as natural sites where reconnection occurs.

Among the reconnection regimes, oscillatory reconnection (OR) represents a particular form of time-dependent reconnection, characterised by periodic changes in magnetic connectivity. The phenomenon was first reported by Craig & McClymont (1991), who analyzed the relaxation of a two-dimensional (2D) X-point magnetic field configuration. OR is characterized by periodic behavior that arises naturally from the system's internal relaxation dynamics rather than from any external periodic driver. This self-sustaining oscil-

lation allows OR to produce quasi-periodic outputs even when the initial perturbations are aperiodic (McLaughlin et al. 2009, 2012).

The connection between OR and wave processes becomes particularly intriguing in regions close to magnetic nulls, where magnetohydrodynamic (MHD) mode conversion can occur. This interaction occurs when Alfvén and sound speeds are comparable, a condition often satisfied near null points. 2D numerical experiments have demonstrated how fast-wave fronts wrap around nulls, leading to energy focusing and complex field behavior (McLaughlin & Hood 2006; Nakariakov et al. 2006; McLaughlin et al. 2011).

The accumulation of fast-wave energy near nulls intensifies wave amplitudes, frequently producing steepening, shocks, and current density enhancements (Nakariakov et al. 2006). Quantitative studies by Tarr et al. (2017) revealed the energy partitioning during such interactions, showing that approximately 70% of incident wave energy converts to slow magnetoacoustic waves, 7% to fast magnetoacoustic waves, with the remaining 23% persisting at the null for eventual dissipation. Recent advances in both simulations and observations have strengthened these findings. Mondal et al. (2024) simulated external perturbations interacting with a 2D coronal null, observing current sheet formation and subsequent plasmoid dynamics that generate fast magnetoacoustic waves.

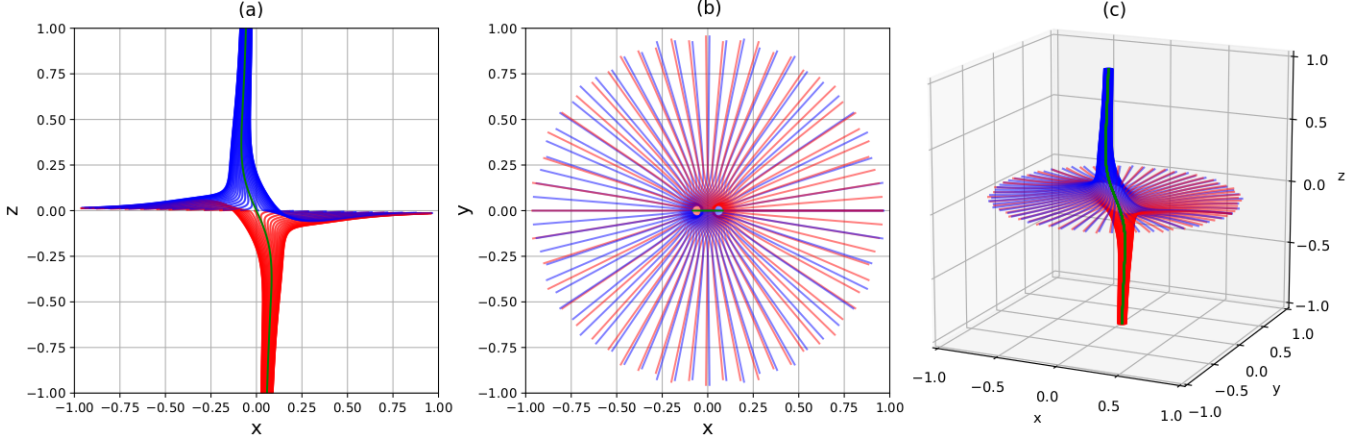


Figure 1. Traced magnetic field lines for the initial condition, panels show different views of the initial condition: (a) a xz -view, (b) a xy -view, (c) 3D view. The green line represents the null point spine, while the blue and red lines represent the fan plane traced from the upper and lower boundaries, respectively.

coustic waves, while Kumar et al. (2024) provided the first observational evidence of fast-to-slow mode conversion at a 3D null point within a pseudostreamer configuration, bridging the gap between theoretical predictions and solar observations.

Moving to three dimensions (3D) introduces additional complexity. In 3D systems, magnetic reconnection can develop in current layers that either contain null points or not, and field lines evolve through continuous slippage rather than discrete reconnection of pairs (Priest et al. 2003). At 3D nulls, reconnection may occur through different modes such as spine-fan, torsional spine, or torsional fan reconnection (Priest & Pontin 2009).

Despite these advances, significant gaps remain in our understanding of time dependent 3D magnetic reconnection. Previous 3D studies have focused on analytical frameworks (Priest & Pontin 2009), steady-state models (Wyper & Jain 2010, 2011), or on tearing-mode simulations (Wyper & Pontin 2014; Huang & Bhattacharjee 2016). The first simulation of OR in 3D was reported by Thurgood et al. (2017), who perturbed a 3D null point using a driver perpendicular to the spine, triggering an oscillatory response. Schiavo et al. (2025) extended these analyses to longer evolution times, demonstrating that the oscillation period remains constant and independent of the driver amplitude. Follow-up simulations by Sabri et al. (2021, 2022) used an Alfvénic driver in similar setups. Building upon these studies, the present work investigates the wave patterns produced throughout the OR cycle.

The paper is organized as follows: §2 details our numerical approach; §3 contains the results, which are divided into the analysis of the OR signature and field line

motion in §3.1, a study of the waves along the spine in §3.2, and fan plane in §3.3; with conclusions in §4.

2. METHODOLOGY AND DIAGNOSTICS

2.1. MHD simulation

The 3D resistive MHD equations are solved using the Lare3D numerical code (Arber et al. 2001). This code employs a Lagrangian predictor–corrector step followed by an Eulerian remap, ensuring conservation of mass, momentum, and energy. In the present study, the response of a 3D magnetic null point was simulated, that is perturbed by a localized spherical magnetoacoustic pulse, which initiates OR.

The governing equations, written in their dimensionless Lagrangian form, are expressed as

$$\frac{D\rho}{Dt} = -\rho \nabla \cdot \mathbf{v}, \quad (1)$$

$$\frac{D\mathbf{v}}{Dt} = \frac{1}{\rho} (\nabla \times \mathbf{B}) \times \mathbf{B} - \frac{1}{\rho} \nabla p + \frac{1}{\rho} \mathbf{F}_{\text{visc}}, \quad (2)$$

$$\frac{De}{Dt} = -\frac{p}{\rho} \nabla \cdot \mathbf{v} + \frac{\eta}{\rho} |\mathbf{j}|^2 + \frac{1}{\rho} Q_{\text{visc}}, \quad (3)$$

$$\frac{D\mathbf{B}}{Dt} = (\mathbf{B} \cdot \nabla) \mathbf{v} - \mathbf{B} (\nabla \cdot \mathbf{v}) - \nabla \times (\eta \nabla \times \mathbf{B}), \quad (4)$$

$$p = \rho e(\gamma - 1), \quad (5)$$

where D/Dt denotes the material derivative, ρ the mass density, \mathbf{v} the velocity field, and \mathbf{B} the magnetic field. The electric current density is given by $\mathbf{j} = \nabla \times \mathbf{B}$, p is the thermal pressure, e is the specific internal energy, η is the magnetic diffusivity, and $\gamma = 5/3$ is the adiabatic index. The viscous force \mathbf{F}_{visc} and the associated heating term Q_{visc} provide numerical stabilization and represent artificial viscous dissipation (Caramana et al. 1998).

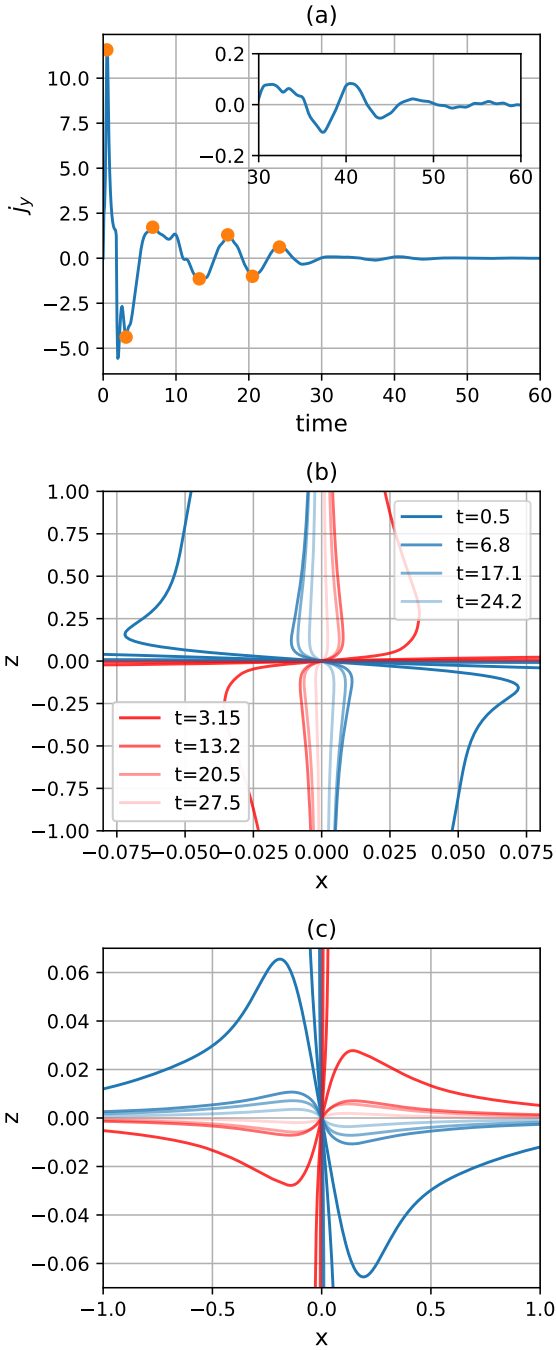


Figure 2. (a) Current density oscillations at the null point, $j_y(0, 0, 0, t)$, showing a signature of oscillatory reconnection, where the blue curve represents the simulated $j_y(0, 0, 0, t)$ and orange dots indicate the simulation times displayed in panels (b)-(c) and Figures 6, 9 and 11. (b) Spine evolution during reconnection cycles, with blue and red curves corresponding to the $j_y(0, 0, 0, t)$ orange dots in panel (a). (c) Fan plane evolution at $y = 0$, using the same color scheme from panel (b) to denote the oscillation phases. Field lines from panels (b)-(c) were traced from the null point.

The system is nondimensionalized by characteristic scales of length L_0 , magnetic field strength B_0 , and mass density ρ_0 , with μ_0 denoting the magnetic permeability of free space. These define the derived units $v_0 = B_0/\sqrt{\mu_0\rho_0}$, $t_0 = L_0/v_0$, $j_0 = B_0/(\mu_0 L_0)$, $p_0 = B_0^2/\mu_0$, and $e_0 = v_0^2$. A detailed explanation for the boundary conditions and setup for this simulation are described in Schiavo et al. (2025).

2.2. Initial magnetic field configuration

The computational domain contains a single 3D magnetic null point located at the origin of a Cartesian coordinate system. The equilibrium field corresponds to a linear, potential, proper null configuration (Parnell et al. 1996). In this geometry, the fan surface coincides with the $z = 0$ plane, while the spine axis aligns approximately with the z -direction. This configuration is identical in form to that used by Thurgood et al. (2017) and Schiavo et al. (2025), and the present work focuses on the associated and generated wave dynamics.

The initial magnetic field is decomposed into a background equilibrium and a perturbation field,

$$\mathbf{B} = \bar{\mathbf{B}} + \mathbf{B}', \quad (6)$$

with

$$\bar{\mathbf{B}} = (x, y, -2z), \quad \mathbf{B}' = \nabla \times \mathbf{A}', \quad (7)$$

and

$$\mathbf{A}' = \psi \exp \left[-\frac{x^2 + y^2 + z^2}{2\sigma^2} \right] \hat{\mathbf{y}}. \quad (8)$$

Here, overbars denote equilibrium quantities and primes indicate perturbations. The decomposition is exact and the perturbations are nonlinear. The equilibrium plasma parameters are uniform, with $\bar{\rho} = 1$, $\bar{\mathbf{v}} = 0$, and $\bar{\rho} = 0.005$, corresponding to a plasma beta of $\beta = 0.01$ at a distance of unity from the null. The resistivity is constant and set to be $\eta = 10^{-3}$.

The perturbation amplitude and spatial extent are controlled by the constants ψ and σ , respectively. Unless otherwise stated, $\sigma = 0.21$ and $\psi = 0.05$ were used, following Thurgood et al. (2017). The perturbation is the same as that in Thurgood et al. (2017) and Schiavo et al. (2025), and is selected to induce a slight bend in the spine relative to the fan, in the xz -plane, aiming to trigger oscillatory spine-fan reconnection. Simulations are evolved for a total time of $60t_0$. Figure 1 shows the resulting magnetic topology based on Eqs. (6)–(8); the perturbation produces a noticeable bending of the spine field lines away from perfect alignment with the z -axis.

2.3. MHD wave proxies in 3D

In a uniform plasma, Alfvén waves are incompressible and are parallel to vorticity, while magnetoacoustic

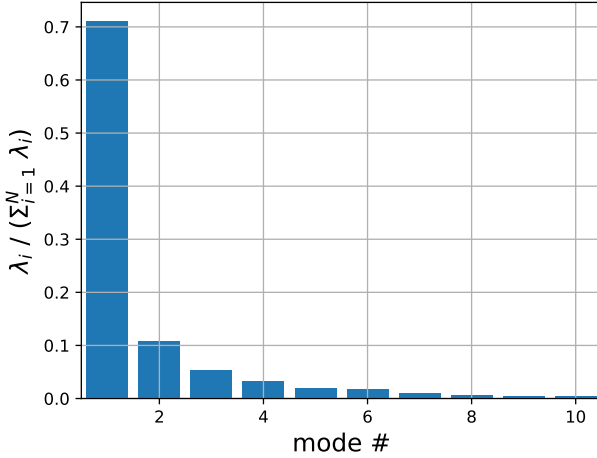


Figure 3. SPOD energy spectra, where mode energy, λ_i , is normalized by the total perturbation energy, $\sum_i^N \lambda_i$.

waves (fast and slow) are compressible waves that in general do have a parallel component of displacement but do not propagate parallel to vorticity (Goossens et al. 2019). In a non-uniform plasma, MHD waves are coupled and can have mixed properties. In low- β plasmas, such as the solar corona, slow magnetoacoustic waves manifest as longitudinal, sound-like disturbances that are aligned with the magnetic field. Fast waves, by contrast, propagate most rapidly in the direction transverse to the magnetic field.

These wave characteristics are quantified using three key identifiers. Following the formalism of Raboonyik (2021) we define three MHD wave-proxies:

$$\xi_A = (\nabla \times \mathbf{v}) \cdot \mathbf{e}_{\parallel}, \quad (9)$$

$$\xi_{\parallel} = \nabla \cdot (v_{\parallel} \mathbf{e}_{\parallel}), \quad (10)$$

$$\xi_{\perp} = \nabla \cdot \mathbf{v} - \xi_{\parallel} = \nabla \cdot (\mathbf{v} - v_{\parallel} \mathbf{e}_{\parallel}). \quad (11)$$

Here, $\mathbf{e}_{\parallel} = \mathbf{B}/|\mathbf{B}|$ is the unit vector parallel to the magnetic field \mathbf{B} . The variable $v_{\parallel} = \mathbf{v} \cdot \mathbf{e}_{\parallel}$ denotes the field-aligned velocity component. These quantities serve as proxies for three distinct wave components and were applied previously on wave identification (Raboonyik 2021; Enerhaug et al. 2024, 2025). These wave-proxies have a physical meaning since they represent: an incompressible parallel component (ξ_A , Eq. 9), a compressible parallel component (ξ_{\parallel} , Eq. 10), and a compressible transverse component (ξ_{\perp} , Eq. 11). These identifiers are not exact representations of the three fundamental MHD wave modes, but they encapsulate the essential features distinguishing wave behavior, and hence are of use in mode identification.

2.4. Spectral Proper Orthogonal Decomposition (SPOD)

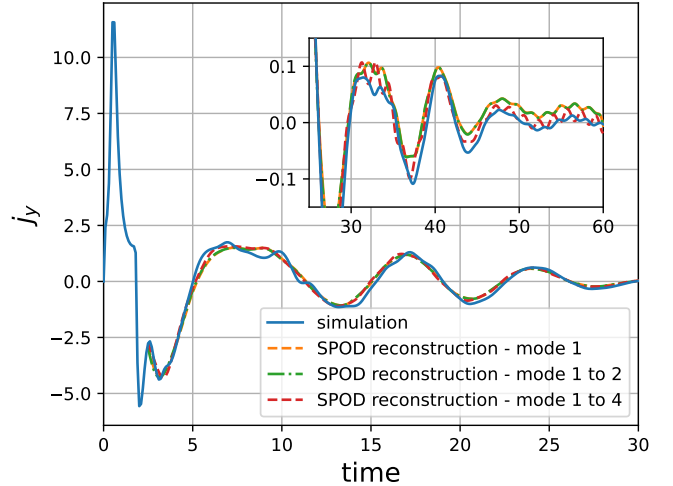


Figure 4. Comparison between simulation and SPOD for the current density measured at the null point.

Proper orthogonal decomposition (POD) is a powerful dimensionality reduction technique that can extract coherent structures from high-dimensional systems. Originally applied by Lumley (1967) for analyzing turbulent fluid flows, this method has demonstrated remarkable success in solar physics applications. It has been used for analysis of large-scale magnetic structures (sunspots and pores) and has enabled the first identification of multiple high-order eigenmodes in photospheric observations (Albidah et al. 2021, 2022; Jafarzadeh et al. 2025). Here SPOD is applied from Sieber et al. (2016), which is an evolution of POD that provides a more statistically robust way to isolate coherent structures within specific frequency bands, compared to POD.

SPOD is especially valuable for analyzing complex, non-stationary systems with inhomogeneous structures. The method's core principle involves decomposing a time series of fluctuating fields, typically represented as discrete snapshots, into a hierarchical series of orthogonal spatial modes. These modes are ranked by their associated eigenvalues, which quantitatively represent each mode's contribution to the total variance (or energy content) of the system. The decomposition yields two key components for each mode: the spatial structures (spatial mode) that reveal coherent patterns, and temporal coefficients that describe the mode's evolution.

Crucially, the eigenvalue spectrum provides immediate physical insight: modes with larger eigenvalues capture more significant contributions to the system's overall dynamics. This ranking enables efficient low-dimensional representations by retaining only the most energetically important modes while still capturing the dominant features of the flow or field evolution. The

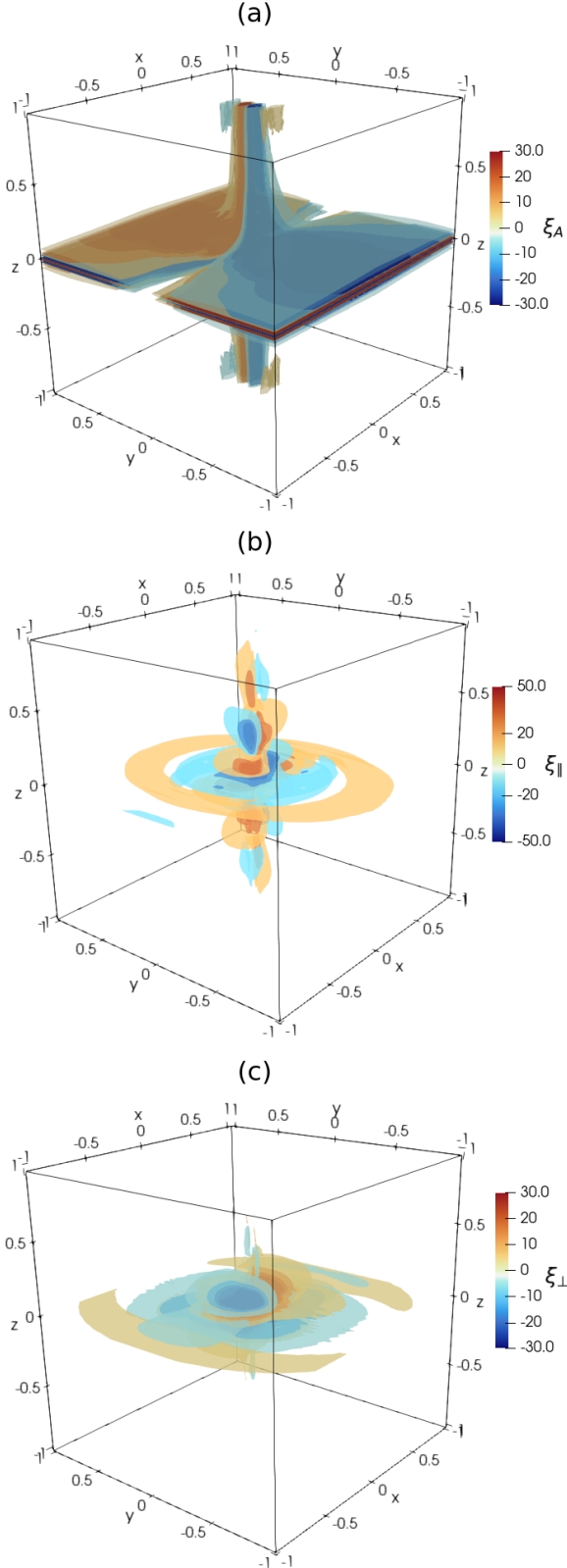


Figure 5. Isosurfaces of SPOD dominant spatial mode $\phi(\mathbf{x})$ for the MHD wave proxies: (a) ξ_A , (b) ξ_{\parallel} and (c) ξ_{\perp} .

decomposition of a vector of variables, \mathbf{Q} , is done as:

$$\mathbf{Q}(\mathbf{x}, t) = \langle \mathbf{Q}(\mathbf{x}) \rangle + \mathbf{Q}''(\mathbf{x}, t), \quad (12)$$

$$\mathbf{Q}''(\mathbf{x}, t) = \sum_{n=1}^N a^{(n)}(t) \phi^{(n)}(\mathbf{x}), \quad (13)$$

where $\phi^{(n)}$ represents a set of space-dependent orthonormal modes, $a^{(n)}$ is a time-dependent mode amplitude, N is the number of snapshots, and n identifies the mode index, $\langle \cdot \rangle$ represents a time average, and the double prime denotes a fluctuation. A reconstructed fluctuation field, represented by $\tilde{(\cdot)}$, can then be approximated by:

$$\tilde{\mathbf{Q}}''(\mathbf{x}, t) \approx \sum_{n=1}^M a^{(n)}(t) \phi^{(n)}(\mathbf{x}), \quad (14)$$

where $M < N$ is the number of modes used in the reconstruction. Note that the time-averaged fluctuation relates to the initial base state fluctuation as $\mathbf{Q}' + \bar{\mathbf{Q}} = \mathbf{Q}'' + \langle \mathbf{Q} \rangle$. Using the snapshots method introduced by Sirovich (1987), the modal basis was constructed using a covariance matrix of the magnetic fluctuation field as:

$$C_{t_1, t_2} = \frac{1}{N} \int_{\Omega} \mathbf{B}''(\mathbf{x}, t_1) \cdot \mathbf{B}''(\mathbf{x}, t_2) d\Omega. \quad (15)$$

Ω is the integration domain, which was chosen to be $-1 \leq x, y, z \leq 1$. Additionally, for computing SPOD a kernel filter was applied to the covariance matrix C (Sieber et al. 2016). In our analysis, we used a Gaussian filter with a bandwidth of 15 snapshots. If we had not applied this filter to C , we would have obtained the standard POD method described by Lumley (1967).

This matrix is symmetric, positive, and semi-definite. Therefore the eigenvalues and eigenvectors are computed using singular value decomposition. The eigenvalue problem $CF = \Lambda F$ is solved, where Λ is a diagonal eigenvalue matrix and F represents the eigenvector matrix of the covariance matrix C . Thus, the SPOD spatial modes were computed by a linear combination of the snapshots into an orthonormal set of basis functions:

$$\phi^{(n)}(\mathbf{x}) = \frac{1}{\lambda_n N} \sum_{k=1}^N F_{k,n} \mathbf{Q}''(\mathbf{x}, t_k), \quad (16)$$

where λ_n is the n^{th} eigenvalue from the diagonal eigenvalue matrix Λ . Finally, the time-dependent mode amplitude is given by:

$$a^{(n)}(t_k) = \sqrt{N \lambda_n} F_{k,n}. \quad (17)$$

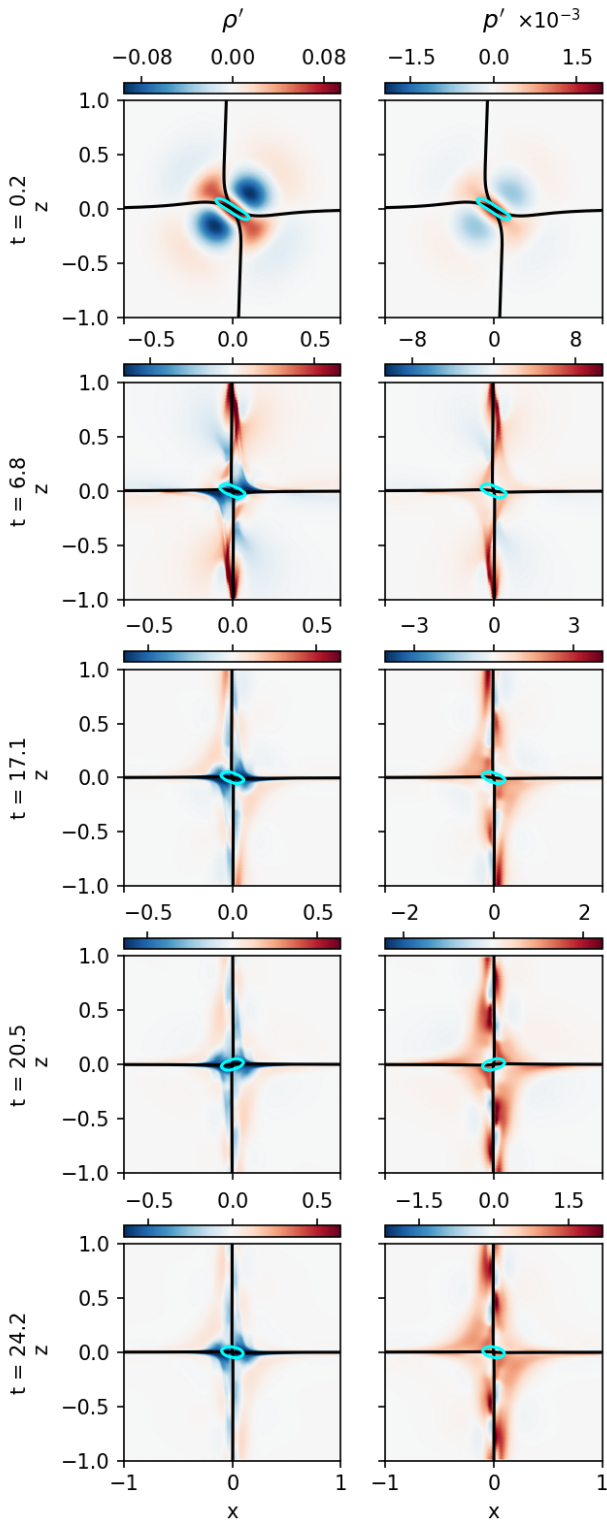


Figure 6. Contour plots in the $y = 0$ plane displaying the time evolution of ρ' and p' . The cyan lines represent the equipartition layer and the black magnetic field lines indicate the magnetic skeleton. The simulation time instants shown were chosen from the orange dots in Figure 2(a).

2.5. Tracing wave paths

To characterize wave propagation time-distance diagrams were created for a specific variable $f(t, S)$ and passive scalar tracers were superimposed on these diagrams. Passive scalar tracers provide insight into the path of a particular wave traveling at a defined reference speed $v_{\text{reference}}$.

The trajectories of the tracers are calculated using a fourth-order Runge-Kutta integration, described by the following equation:

$$\frac{dS}{dt} = v_{\text{reference}}(t, S) \quad (18)$$

where the variable S can represent the coordinate along the spine, the x -axis, the y -axis, or any other specific line. The reference speed $v_{\text{reference}}(t, S)$ depends on space and time, calculated with the local properties of the full solution.

The reference speed $v_{\text{reference}}$ could be the local sound speed $v_s = \sqrt{\gamma p / \rho}$, the Alfvén speed $v_A = |\mathbf{B}| / \sqrt{\mu_0 \rho}$, or either the fast \mathbf{c}_f or slow \mathbf{c}_s magnetoacoustic velocities. The components of the magnetoacoustic velocities in 3D are defined as follows:

$$c_{f,i}^2 = \alpha + \sqrt{\alpha^2 - v_s^2 \frac{B_i^2}{\mu \rho}}, \quad (19)$$

$$c_{s,i}^2 = \alpha - \sqrt{\alpha^2 - v_s^2 \frac{B_i^2}{\mu \rho}}, \quad (20)$$

where $\alpha = (v_s^2 + v_A^2)/2$ and B_i is magnetic field vector in the direction i (see [Raboonik et al. \(2024\)](#)). propagation

3. RESULTS

3.1. OR signature and field line motion

The signature of OR is characterized by the oscillatory behavior of the current density at the null point. In this simulation, it was found that the null point remains stationary, located at $x = y = z = 0$, as determined by the null point identification algorithm described in [Haynes & Parnell \(2007\)](#). Figure 2a shows the signature of OR measured over $t = 60$ (with $t = 60$ in nondimensional units). When j_y changes its sign, the current sheet is reoriented, as discussed by [McLaughlin et al. \(2009\)](#).

Early in the simulation (at $t = 0.4$) there is a significant overshoot in $j_y(0, 0, 0, t)$, caused by the initial perturbation. After one complete reconnection cycle, around $t \approx 5$, the influence of the initial perturbation diminishes. At this point, $j_y(0, 0, 0, t)$ exhibits a more regular oscillatory behavior with a constant frequency and Gaussian decay, as noted by [Schiavo et al. \(2025\)](#). The $j_y(0, 0, 0, t)$ oscillation period P is approximately

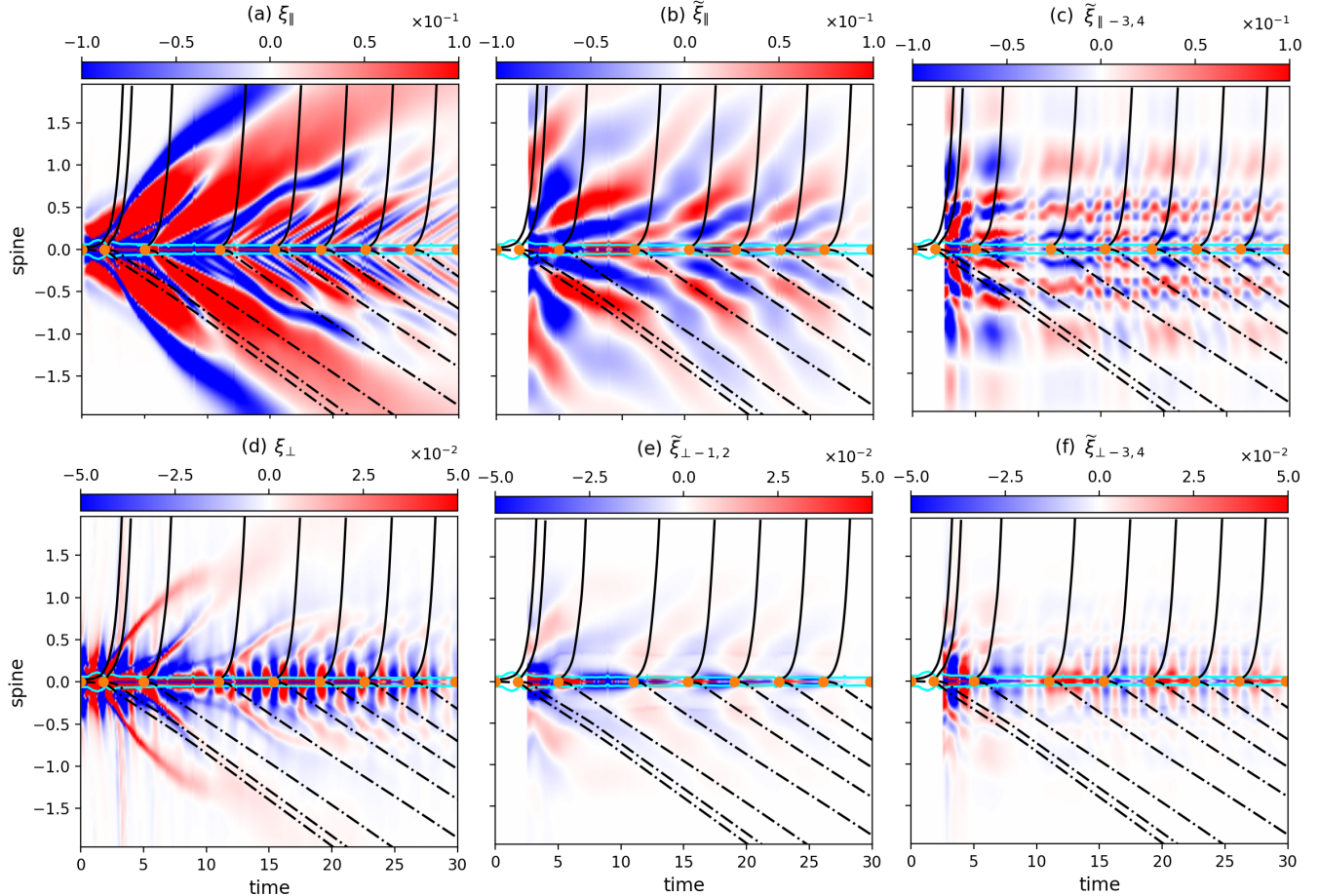


Figure 7. Time-distance diagrams for ξ_{\parallel} and ξ_{\perp} and their SPOD reconstruction along the spine. The orange dots mark the roots of $j_y(0,0,0,t)$, while cyan lines indicate the equipartition layer. The black dashed-dotted and black continuous lines represent the slow and fast magnetoacoustic wave trajectories.

constant, where Schiavo et al. (2025) found the period to be $P = (8.1 \pm 1.1)t_0$.

Figures 2b and 2c illustrate the evolution of the spine and fan during the reconnection cycle. The time instants shown in these figures correspond to the peaks and valleys of $j_y(0,0,0,t)$ marked as orange dots in Figure 2a. Peaks are marked with blue lines, while red lines represent valleys in Figures 2b and 2c.

The current sheet size decreases significantly after the first reconnection cycle, as seen in Figures 2b and 2c, as well as the current density amplitude (Figure 2a). This reduction is particularly noticeable after $t = 3.2$. Before this time, the initial pulse heavily influences the dynamics (seen in $t = 0.5$ and 3.2). Following the first cycle, the oscillations of $j_y(0,0,0,t)$ exhibit a Gaussian decay, as described by Schiavo et al. (2025). These oscillations lead to deformations in the fan plane, which can create propagating disturbances along it. A more detailed analysis of these waves will be presented in the upcoming sections.

SPOD was employed to disentangle perturbation dynamics into coherent modes. The decomposition was computed using 275 simulation snapshots spanning $t = 2.5$ to 30, with the initial time explicitly chosen to avoid contamination from the initial pulse in the SPOD modal basis.

Figure 3 displays the normalized energy contribution of the first 10 most energetic SPOD modes, where each eigenvalue represents the mode's energy fraction relative to the total fluctuation energy. This result was obtained by integrating over the cube $-1 \leq x, y, z \leq 1$ that surrounds the null point. The histogram reveals three key findings: firstly, mode 1 dominates the system, accounting for approximately 73% of the total fluctuation energy that corresponds to the OR dynamics. Secondly, the first four modes collectively account for approximately 90% of the system's fluctuations. Thirdly, higher modes show rapidly decreasing energy contributions, suggesting their minor role in the overall dynamics.

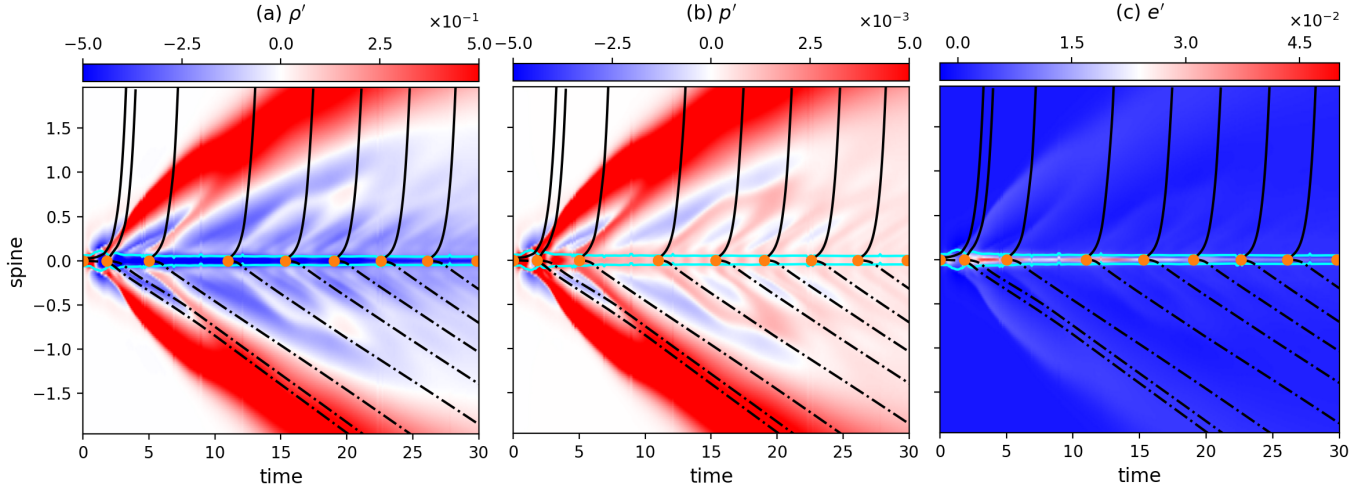


Figure 8. Time-distance diagrams showing (a) density, (b) pressure and (c) energy perturbations along the spine. The orange dots mark the roots of $j_y(0,0,0,t)$ in Figure 2a, while cyan lines indicate the equipartition layer. The dashed-dotted lines represent trajectories propagating at the local slow magnetoacoustic speed and black continuous lines represent fast magnetoacoustic speed trajectories.

Figure 4 compares $j_y(0,0,0,t)$ with the SPOD reconstructions, $\tilde{j}_y(0,0,0,t)$, using only mode 1, as well as modes 1 and 2, and modes 1 to 4 respectively. The reconstruction using only mode 1 closely matches the oscillation pattern of $j_y(0,0,0,t)$, with minor differences. This indicates that mode 1 is sufficient to describe the $\tilde{j}_y(0,0,0,t)$ signature at the null. Including modes 2, 3, and 4 results in only slight improvements in the representation of $\tilde{j}_y(0,0,0,t)$.

Figure 5 presents isosurface visualizations of the dominant SPOD mode (mode 1) for each MHD wave proxy: ξ_A , ξ_{\parallel} and ξ_{\perp} described by Eqs. (9)-(11).

For ξ_A (Figure 5a), associated with incompressible waves, the perturbation mainly occurs in the fan plane with symmetric distribution about $y = 0$. The mode exhibits two non-propagating rolls around the spine, consistent with Schiavo et al. (2025), that found these vorticity rolls generated by the spine motion, do not propagate along the z direction. The ξ_{\parallel} perturbation (Figure 5b) demonstrates two characteristic features, circular wave patterns in the fan plane and oscillatory behavior along the spine (z -axis). This spatial structure suggests coupling between fan plane and spine dynamics, since the oscillations are present in the same mode. The ξ_{\perp} mode (Figure 5c) shows more localized behavior, concentrated near the null point and fan plane. In contrast to the parallel perturbations, ξ_{\parallel} , the transverse perturbations do not extend along the z -axis (the spine).

3.2. Wave propagation around the spine

Figure 6 illustrates contour plots of density and pressure perturbations, defined as ρ' and p' . The figure rep-

resents evolution along the $y = 0$ plane, which is a symmetry plane.

At $t = 0.2$, the initial perturbation generates pressure and density disturbances propagating toward the null point, perturbing the base state. By $t = 6.8$, after the initial pulse has reached the null point and the completion of a single reconnection cycle, there are large perturbations that travel along the spine. At $t = 17.1$, during the second reconnection cycle, a distinct wave pattern forms along the spine with a shorter wavelength than that seen at $t = 6.8$. It is noteworthy that these pulses are observed in both density and pressure, indicating they are magnetoacoustic waves. The subsequent panels at $t = 20.5$ and $t = 24.1$ show a similar emission pattern to that observed at $t = 17.1$ but with reduced amplitude. Note that the density perturbation amplitude remains similar after the initial transient ($t \leq 6.8$), while the pressure perturbation reduces by approximately half after each reconnection cycle ($t = 6.8, 17.1$ and 24.2).

Additionally, it is significant to highlight that the wave emissions (Figure 6) are synchronized with the OR fingerprint from j_y (Figure 2a), suggesting that these waves may be generated by the OR, potentially due to reconnection jets reforming in a periodic manner.

3.2.1. Wave propagation along the spine

After characterizing OR (j_y at the null point) and wave propagation patterns along the spine, we move the focus to MHD wave types. Two complementary approaches are used to identify the waves: time-distance diagrams tracking perturbation evolution along characteristic field lines for the wave proxies, and the wave tracers discussed in §2.5.

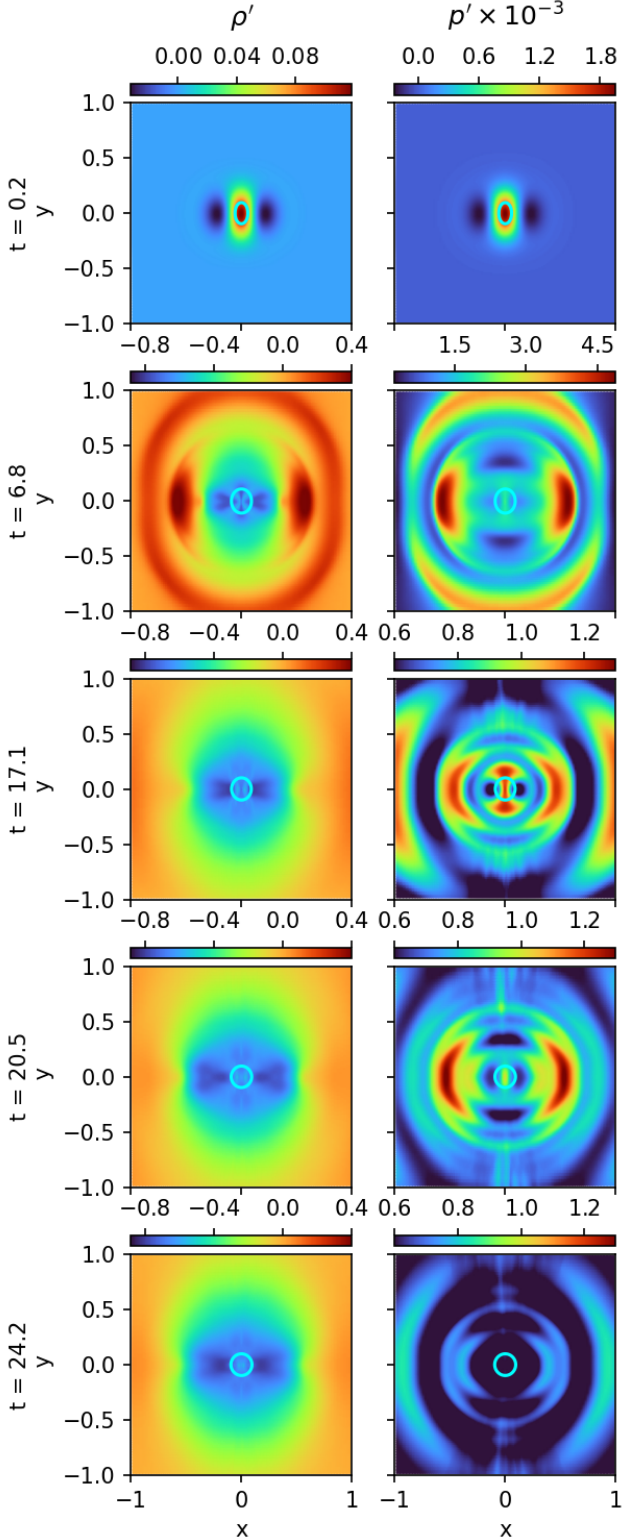


Figure 9. Contour plots in the $z = 0$ plane (fan plane) displaying the evolution of ρ' and p' . The cyan lines represent the equipartition layer, and the simulation time instants shown were chosen from the orange dots in Figure 2a.

Regarding the analysis of the MHD wave proxies, Figure 7 presents present time-distance diagrams for compressible parallel and transverse wave proxies, ξ_{\parallel} and ξ_{\perp} , with their SPOD reconstructions, $\tilde{\xi}_{\parallel}$ and $\tilde{\xi}_{\perp}$. ξ_A (incompressible, Alfvén-like waves) were omitted from Figure 7, since no signal was found propagating along the spine. Here we use pairs of modes for reconstructing propagating waves. According to (Taira et al. 2017) POD and SPOD modes that are real do not contain information of the wave phase (since there is no imaginary part). Instead, they require the superposition of a pair of modes with a phase shift for describing any propagating wave.

The first proxy ξ_{\parallel} in Figure 7a shows compressible perturbations parallel to the magnetic field. There is an initial transient from $t = 0$ to 10, and approximately after the middle of the second reconnection cycle, the propagation (at the third orange dot) starts to develop fully. Additionally, there is no information traveling at the fast speed (black continuum lines) in ξ_{\parallel} .

Figures 7b and 7c present SPOD reconstructions of ξ_{\parallel} using modes 1-2 and modes 3-4, respectively. The modes 1-2 reconstruction (Figure 7b) reveals a wave traveling with the slow speed (dashed-dot lines) and starts at the $j_y(0, 0, 0, t)$ roots (shown as orange dots, i.e. the roots in Figure 2a) with period P .

The modes 3-4 reconstruction (Figure 7c) identifies previously unobserved short-period waves, with periodicity $P/2$, with a significant interference pattern effect (within the range $z \approx \pm 0.5$). It is unclear if these are standing or propagating waves, due to the strong interference pattern. Outside of $z \approx \pm 0.5$, the periodicity becomes P and the waves propagate at the fast magnetoacoustic speed. These features were absent in the original diagram (Figure 7a) which demonstrates the utility of SPOD.

Figure 7d shows compressible transverse perturbations by monitoring ξ_{\perp} , and Figures 7e and 7f present SPOD reconstructions of ξ_{\perp} using modes 1-2 and modes 3-4, respectively. Figure 7d shows that, during the initial transient, from $t = 0$ to 10, there are compressible transverse waves with period $P/2$ traveling with the fast speed (black continuum lines) along the spine, which are not seen after $t = 10$.

The reconstruction using modes 1-2 (shown in Figure 7e) reveals propagating waves, traveling at the slow speed, with period P , i.e. synchronized with the $j_y(0, 0, 0, t)$ roots (Figure 2a).

In contrast, the modes 3-4 reconstruction (Figure 7f) uncovers shorter period, $P/2$, standing waves, that decay rapidly at $z \approx \pm 0.5$. Waves outside this are rapidly damped, i.e. outside $z \approx \pm 0.5$.

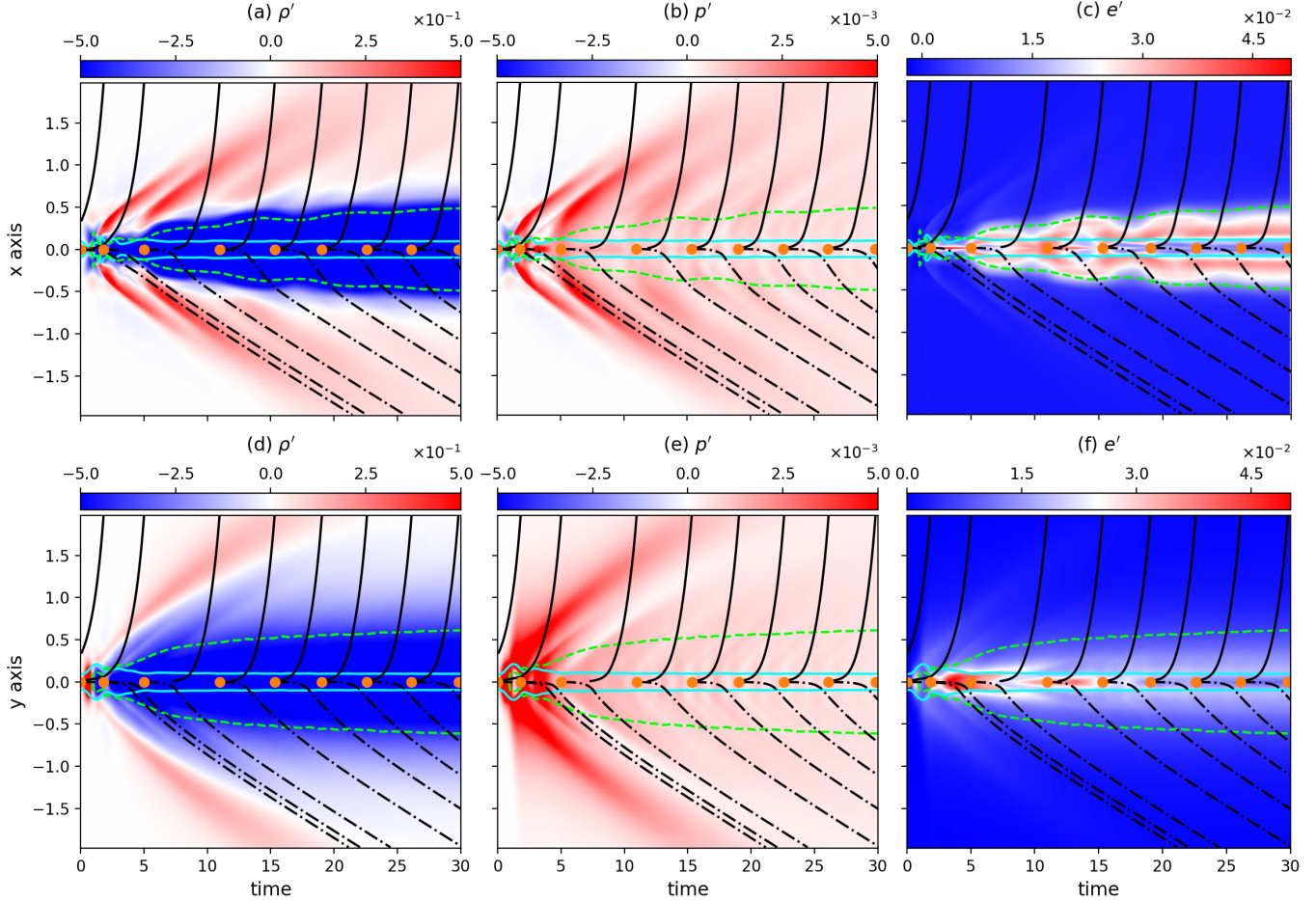


Figure 10. Time-distance diagrams showing ρ' , p' , and e' perturbations along the x -axis and y -axis. The orange dots mark the roots of $j_y(0,0,0,t)$, while cyan lines indicate the equipartition layer and green lines the cavity envelope. The black dashed-dotted and black continuous lines represent the slow and fast magnetoacoustic wave trajectories respectively.

In order to explain the bounding of the standing waves in Figure 7c and 7f), Figure 8 shows the time-distance diagrams along the spine for ρ' , p' and e' .

Figure 8a shows the propagation of waves at the slow speed. From $t = 5$ onward a density depletion forms and move at the slow speed along the spine to approximately ± 1 . Later, from $t = 10$ onward, a series of depletions form at the null and move to ± 0.5 . A similar behavior is seen in Figure 8b for p' . Notice that there is no signature of this in the perturbed energy in Figure 8c. These density and pressure depletions provide the inhomogeneity in the plasma medium that cause the standing waves seen in Figure 7c and 7f, as well as the waves traveling at the slow speed in Figure 7a and 7b.

3.3. Waves in the fan plane

3.3.1. The cavity

Our investigation now turns to the fan plane, which is approximately located at $z = 0$ and oscillates around this position (Figure 2c). As opposed to the spine, the

field line tracing in the fan plane is more complex because they diverge at the null point and are not anchored to any particular position during the system's evolution.

Figure 9 displays contour plots of ρ' and p' that represent evolution along the $z = 0$ plane, which is approximately the fan plane. At $t = 0.2$, the initial transient generates pressure and density disturbances that travels towards the null point. Following the arrival of the initial pulse at the null point, as can be seen at $t = 6.8$, a circular wave is emitted within the fan plane (xy -plane, $z = 0$). The first wavefront, associated with the initial perturbation, is strongest along the y -direction and is located near $x = 0$, $y = \pm 1$, and a second wavefront at $y = 0$, $x = \pm 0.5$, where both waves disturbs the density and pressure. Later in time, at $t = 17.1$, wavefronts are observed near $x = \pm 0.5$, $y = 0$ that exhibit stronger amplitudes in p' along the x -direction and also disturb the density.

After $t = 17.1$, the wave pattern in the fan plane persists but is now predominant along the x -direction.

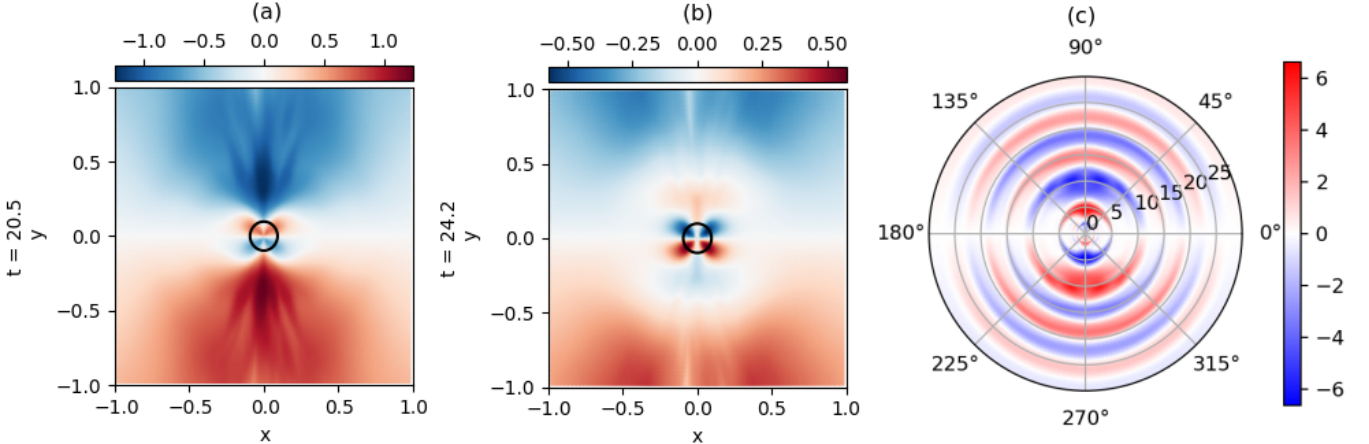


Figure 11. (a) and (b) are contour plots in the $z = 0$ plane displaying the time evolution of the ξ_A . The black circles represent the equipartition layer. The simulation time instants shown here were selected from the orange dots in Figure 2. (c) Polar time-distance diagram for ξ_A in the fan plane where the radial direction represents the simulation time. ξ_A is monitored at a circular line with coordinates $(r = 0.1, \theta, z = 0, t)$.

Subsequent snapshots at $t = 20.5$ and $t = 24.1$ reveal a similar pattern in p' , though with a reduced amplitude. The influence of pressure perturbations on the density after $t = 6.8$ is not visible in the ρ' contour. After $t = 6.8$ the evolution produces a significant density depletion within the fan plane. This depletion is localized to a region approximately within $\sqrt{x^2 + y^2} < 0.5$ and is non-axisymmetric, resulting in a density drop of 70–80%. This indicates the generation of a cavity inside the fan plane ($z = 0$) at $\sqrt{x^2 + y^2} < 0.5$.

The evolution of the thermodynamic variables are analyzed in more detail in the fan plane in Figure 10. The dashed-dotted lines in Figure 10 represent tracers based on the slow magnetoacoustic speed, while the solid lines correspond to the fast magnetoacoustic speed. A green dashed line denotes the boundary of the evolving cavity. This cavity profile was determined by applying a Gaussian fit to the density distribution near the null point at each time step of the time-distance diagram, the cavity boundary is defined as the standard deviation of the Gaussian function.

Along the x -axis (Figures 10a-10c), there is a sharp drop in density perturbation within the cavity region (Figure 10a) and wave generation occurs outside this cavity shell. In contrast, the pressure perturbation diagram (Figure 10b) shows perturbations that originate at the null point. Figure 10c highlights that perturbed internal energy is predominantly confined within the cavity, thus heating the plasma around the null point. Figures 10d-10f exhibit similar behavior along the y -axis, albeit with some differences: the density profile transitions more smoothly across the cavity boundary (Figure 10d) compared to the x -axis (Figure 10a), which is consistent with the earlier analysis in Figure 9. The pres-

sure perturbations (Figure 10e) show a pattern similar to that observed along the x -axis. However, the internal energy perturbations (Figure 10f) reveal a notable contrast. The heating along the y -axis is less intense since the reconnection jets are aligned with the $y = 0$ plane and remain stronger within the equipartition layer. It also display a peak of heat at $t = 7$, after the first reconnection cycle. In contrast, heating along the x -axis is more widely distributed throughout the cavity.

3.3.2. Incompressible waves (ξ_A)

Figure 11a-b illustrates the time evolution of the MHD Alfvén wave proxy ξ_A near the fan plane, at $z = 0$, and are shown over two reconnection cycles, at $t = 20.5$ and 24.2 , corresponding to the last two orange dots in the $j_y(0, 0, 0, t)$ time series (Figure 2a).

The evolution of ξ_A indicates the presence of an incompressible field-aligned vorticity propagating in the fan plane along the y -axis. This wave is perpendicular to the spine motion, which occurs in the xz -plane at $y = 0$ (see Figure 2b). The bending of the fan plane at $y = 0$ (as shown in Figure 2c) generates vorticity that aligns with the magnetic field, resulting in ξ_A . The oscillation period of ξ_A appears to be synchronized with $j_y(0, 0, 0, t)$, supporting the conclusion that ξ_A originates from the bending of the fan plane. Notably, the wave pattern appears to be influenced by the cavity at $t = 24.2$, where the pattern is contained at boundary defined by $\sqrt{x^2 + y^2} \approx 0.5$.

Figure 11c presents a polar time-distance diagram for ξ_A in the fan plane, specifically for a circular path at a constant radius, $\xi_A(r = 0.1, \theta, z = 0, t)$. The contour plot indicates that there is no propagation of incompressible waves along the x axis ($\theta = 0^\circ$ and 180°).

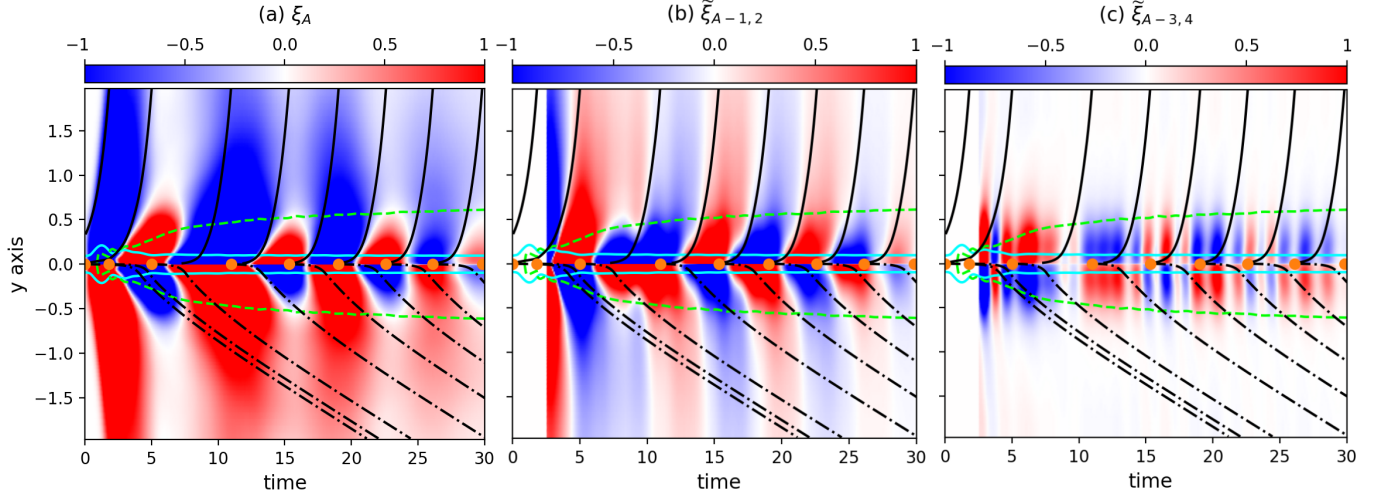


Figure 12. Time-distance diagrams showing for (a) ξ_A and (b) and (c) its SPOD reconstructions, $\tilde{\xi}_A$, along the y -axis. The orange dots mark the roots of $j_y(0, 0, 0, t)$ in Figure 2a, while cyan lines indicate the equipartition layer and green lines the cavity envelope. The black dashed-dotted and black continuous lines represent the slow and fast magnetoacoustic wave trajectories respectively.

Instead, wave propagation is predominantly along the y axis ($\theta = 90^\circ$ and 270°), which aligns with the direction of the current density vector at the null ($\mathbf{j} = (0, j_y, 0)$ see Figure 2a). The polar time-distance diagram shows a dipole pattern and agrees with the behavior seen in Figure 11a-b. Note that $j_y(0, 0, 0, t)$ in Figure 2a changes sign as OR evolves in time and this pattern is repeated by ξ_A inside the equipartition layer, as can be seen in Figures 11a-b.

Figures 12a-12c present time-distance diagrams along the y -axis for ξ_A , as well as its SPOD reconstructions of $\tilde{\xi}_A$ using modes 1-2 and 3-4. These SPOD modes are used to study wave signals and disentangle the complex dynamics into fundamental components, aiding in identifying the origin of each wave mode in the system. In Figure 12, the continuous lines represent the trajectories of the fast speed, while the dashed-dot lines indicate the trajectories of the slow speed.

Figure 12a shows that a wave exists in the system, propagating mainly in the y -direction at the fast speed. The wave signal originates at the null point and has the same period as $j_y(0, 0, 0, t)$, i.e. a period of P . Magnetic reconnection creates movement of the spine in the $y = 0$, xz -plane, which results in the bending of the fan plane (Figure 2c). This bending generates an incompressible wave that propagates transverse to the spine movement in the fan plane along the y -direction. Moreover, the incompressible waves are observed to be more intense within the cavity, and some pulses appear to be contained inside of it.

Figures 12b and 12c provide SPOD reconstructions for the incompressible wave proxy. A comparison between the original data (Figure 12a) and the modes 1-2 re-

construction (Figure 12b) reveals a previously obscured wave propagation beyond the cavity (indicated by the green dashed lines) with a period of P . These waves originate at the null point, exhibit maximum amplitude within the cavity, and propagate outward with diminishing intensity. The modes 3-4 reconstruction (Figure 12c) shows standing waves inside the cavity with periods $P/2$. These standing waves also propagate outward across the cavity boundary but then experience rapid amplitude decay.

3.3.3. Compressible waves in the fan plane

ξ_{\parallel} and ξ_{\perp} are employed to investigate compressible wave motion in the fan plane. Figure 13 illustrates the wave patterns for ξ_{\parallel} and ξ_{\perp} near the fan plane, specifically at $z = 0$ and $t = 24.2$, after two reconnection cycles, and a polar time distance diagram for both variables.

Figure 13a contains contour plots of $\xi_{\parallel}(x, y, 0, t = 24.2)$. This contour plot shows that circular compressible waves exist outside the equipartition layer (i.e., where $\beta < 1$). Outside this layer, a wave pattern propagates radially across the fan plane at $z = 0$. Three distinct patterns are observable in this case. While some dynamics occur within the equipartition layer (where $\sqrt{x^2 + y^2} \lesssim 0.1$), the pattern is not clearly defined in the contour plot. Inside the equipartition layer it is seen that ξ_{\parallel} has the same sign of $j_y(0, 0, 0, t = 24.2)$ (Figure 2a). Beyond this layer however, a well-defined wave pattern emerges, with wave propagation observed up to $\sqrt{x^2 + y^2} \approx 0.5$, which is approximately the cavity boundary, beyond which their wavelength increases.

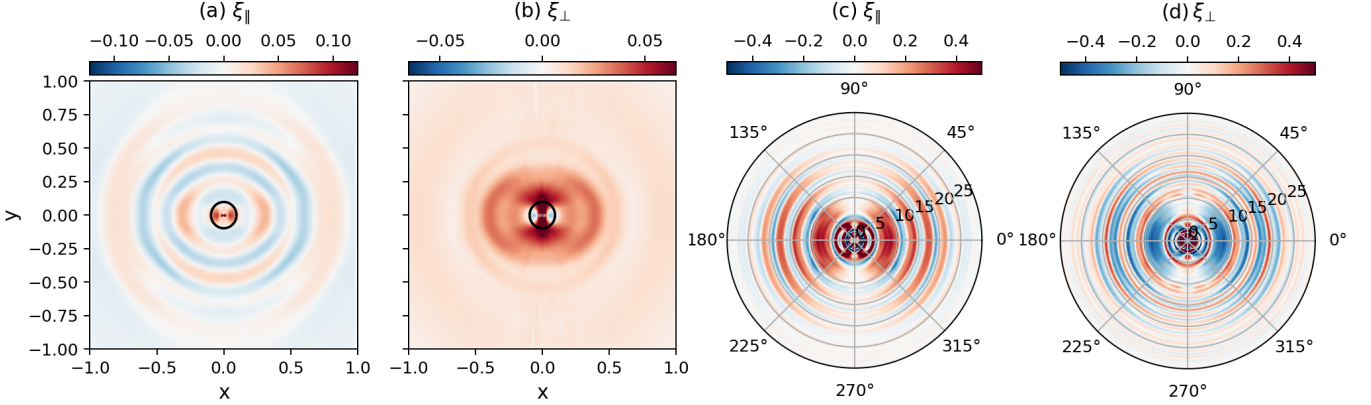


Figure 13. Panels (a) and (b) show the compressible wave proxies in the fan plane, $z = 0$, at $t = 24.2$. The black circle represent the equipartition layer. Panels (c) and (d) show a polar time-distance plot for the compressible wave proxies obtained at $(r = 0.1, \theta, z = 0, t)$, where the radial direction represents the simulation time.

This behavior is mainly created by the perturbations in the fan plane shown in Figure 5b.

Figure 13b presents a contour plot of $\xi_{\perp}(x, y, z = 0, t = 24.2)$. Here, $\xi_{\perp}(x, y, 0, 24.2)$ exhibits a circular wave signal between the equipartition layer and the cavity boundary (where $\sqrt{x^2 + y^2} \approx 0.5$), which may be attributed to fast magnetoacoustic waves. The amplitudes of these waves are smaller than those of ξ_{\parallel} and 10 times smaller than ξ_A . Also from the contour panel, it is unclear whether waves from ξ_{\perp} propagate beyond the cavity or if their amplitude diminishes, rendering them undetectable. Inside the equipartition layer, it is observed that ξ_{\perp} shares the opposite sign as $j_y(0, 0, 0, t = 24.2)$ (Figure 2a) while ξ_{\parallel} has the same sign in the same region.

Figures 13c and 13d present polar time-distance diagrams for ξ_{\parallel} and ξ_{\perp} along a line at $\sqrt{x^2 + y^2} = 0.1$, outside the equipartition layer and inside the cavity, and $z = 0$. Figure 13c shows that ξ_{\parallel} exhibits a circular waves that are non-uniform in the polar direction; it oscillates between -0.5 and 0.5, with a reduction in the amplitude along the y -axis (at $\theta = 90^\circ$ and 270°), where it oscillates between -0.2 and 0.2. The oscillation amplitudes are higher along the x -axis (at $\theta = 0^\circ$ and 180°). In figure 13d, ξ_{\perp} displays a circular wave pattern where the wave amplitude is higher along the x -axis (at $\theta = 0^\circ$ and 180°). The propagation along the y -axis (at $\theta = 90^\circ$ and 270°) are observed but are less intense, showing only positive values, while along the x -axis it oscillates between -0.5 to 0.5.

3.3.4. Compressible waves along the y -axis

The next analysis moves to the evolution along the y -axis in the fan plane. Figures 14a to 14f present time-distance diagrams for compressible parallel and trans-

verse wave proxies, ξ_{\parallel} and ξ_{\perp} , with their SPOD reconstructions, $\tilde{\xi}_{\parallel}$ and $\tilde{\xi}_{\perp}$.

Figure 14a illustrates the compressible parallel perturbations, ξ_{\parallel} , along the y -axis in the fan plane. Between $t = 0$ and 10, there is an initial transient and the formation of the low-density cavity (dashed green line). After the initial transient, short-period oscillations within the cavity propagate at a slow speed, at a period of approximately $P/2$, and terminate at the cavity boundary. Outside the cavity, there are compressible waves that are synchronized with $j_y(0, 0, 0, t)$ roots in Figure 2a with a period of P and traveling at the slow speed (following the dashed-dot paths). This confirms the results in Figure 13a.

Figures 14b and 14c present SPOD reconstructions using modes 1-2 and modes 3-4, respectively. The modes 1-2 reconstruction (Figure 14b) confirms the synchronization with the $j_y(0, 0, 0, t)$ roots in Figure 2a and verifies the propagation of slow magnetoacoustic waves beyond the cavity.

Figure 14c shows the modes 3-4 reconstruction. Within the cavity, short-period waves with periodicity $P/2$ are observed, propagating at the local slow speed. Outside the cavity, these waves propagate at the fast magnetoacoustic speed with period P .

Figure 14d, shows the transverse compressible perturbations in ξ_{\perp} . The transverse perturbations exhibit behavior similar to that seen along the spine (as shown in Figure 7d). During the initial transient, $t = 0$ to $t = 10$, oscillations are displaying shorter periods than the OR period, specifically a period of $P/2$ between $y \pm 0.5$ to 2 (following fast magnetoacoustic speed black lines).

Figures 5c and 13b emphasize that the perturbation is contained mainly inside the cavity.

Figures 14e and 14f compare SPOD reconstructions using two different combinations of modes: modes 1-

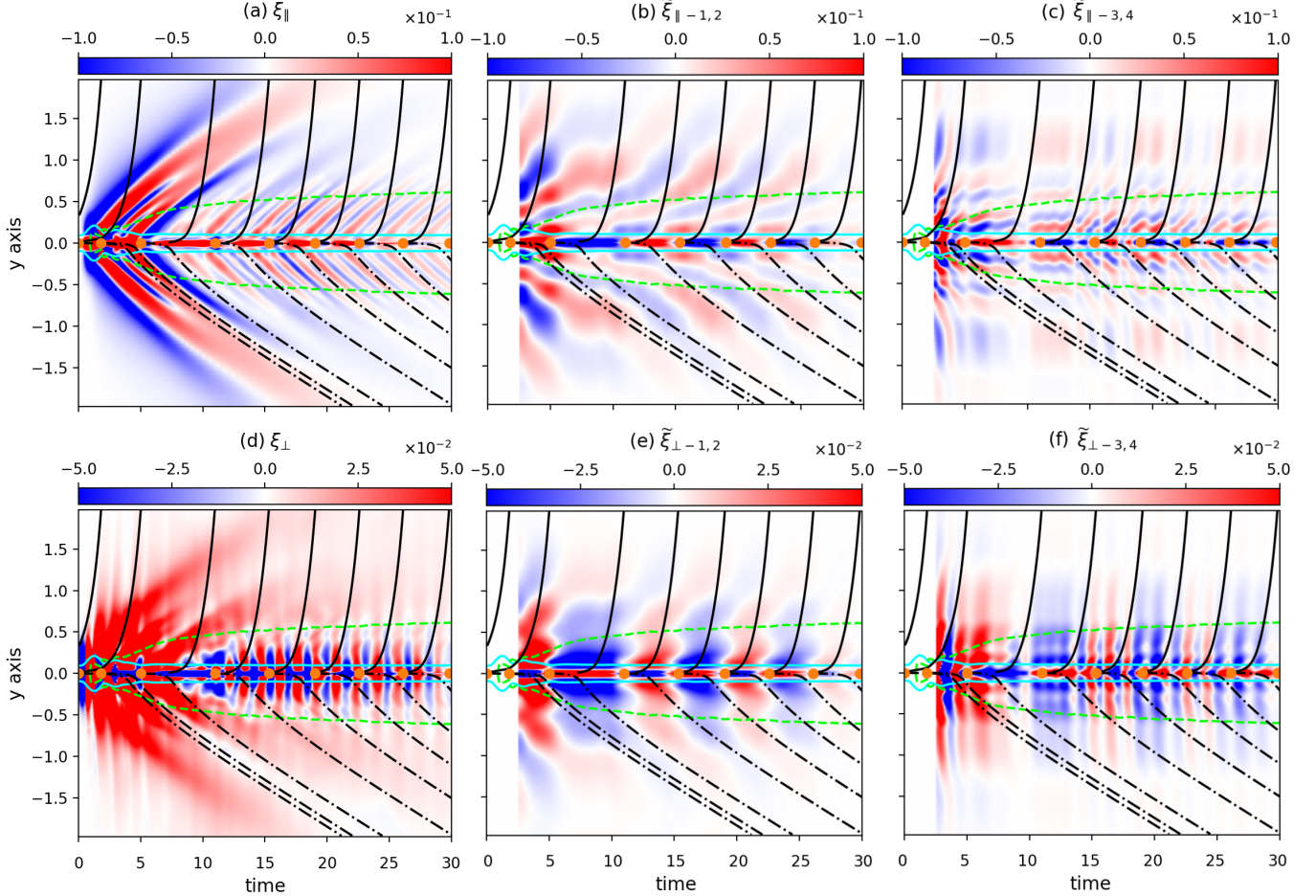


Figure 14. Time-distance diagrams for ξ_{\parallel} and ξ_{\perp} and their SPOD reconstruction along the y -axis. The orange dots mark the roots of $j_y(0,0,0,t)$, while cyan lines indicate the equipartition layer and green lines the cavity envelope. The black dashed-dotted and black continuous lines represent the slow and fast magnetoacoustic wave trajectories respectively.

2 and modes 3-4. The reconstruction using modes 1-2 (shown in Figure 14e) reveals propagating waves synchronized with the $j_y(0,0,0,t)$ roots (Figure 2a) within and outside the cavity.

In contrast, the modes 3-4 reconstruction (Figure 14f) uncovers $P/2$ cavity-trapped, standing oscillations. Waves outside the cavity (i.e. outside $y = \pm 0.5$) propagate at the fast magnetoacoustic speed (following the black continuous lines) but they decay rapidly.

3.3.5. Compressible waves along the x -axis

Finally, the compressible wave proxies along the x -axis are investigated. The results can be seen in Figure 15, which shows the time-distance diagrams for ξ_{\parallel} and ξ_{\perp} and their SPOD reconstruction along the x -axis. The results are very similar to those in §3.3.4, for example Figure 15b reports a wave traveling with the slow speed (dashed-dot lines) with period P , and thus the behavior is reminiscent of that observed for the same variable along the spine (Figure 7b) and y -axis (Figure

14b). Thus, the full breakdown of the results in Figure 15 is not repeated here.

4. CONCLUSIONS

The investigation of wave generation at a 3D magnetic null point reveals several key insights into the coupling between oscillatory reconnection (OR) and magnetohydrodynamic (MHD) wave dynamics. The analysis demonstrates that OR serves as a robust mechanism for generating self-sustained oscillations, even when initiated by a single aperiodic perturbation. The periodic reversals in current density at the null point, synchronized with fan plane deformations, drive a rich spectrum of MHD waves across the spine and fan structures.

The OR signature is quantified by $j_y(0,0,0,t)$. Its roots (Figure 2a) determines a characteristic period, P , in the system. Wave motions of period P and $P/2$ are observed in the system (see below). $j_y(0,0,0,t)$ exhibits a Gaussian decay, as discussed in Schiavo et al. (2025). It was tracked via the motion of the spine and fan plane in the xz -plane at $y = 0$. It was demonstrated that

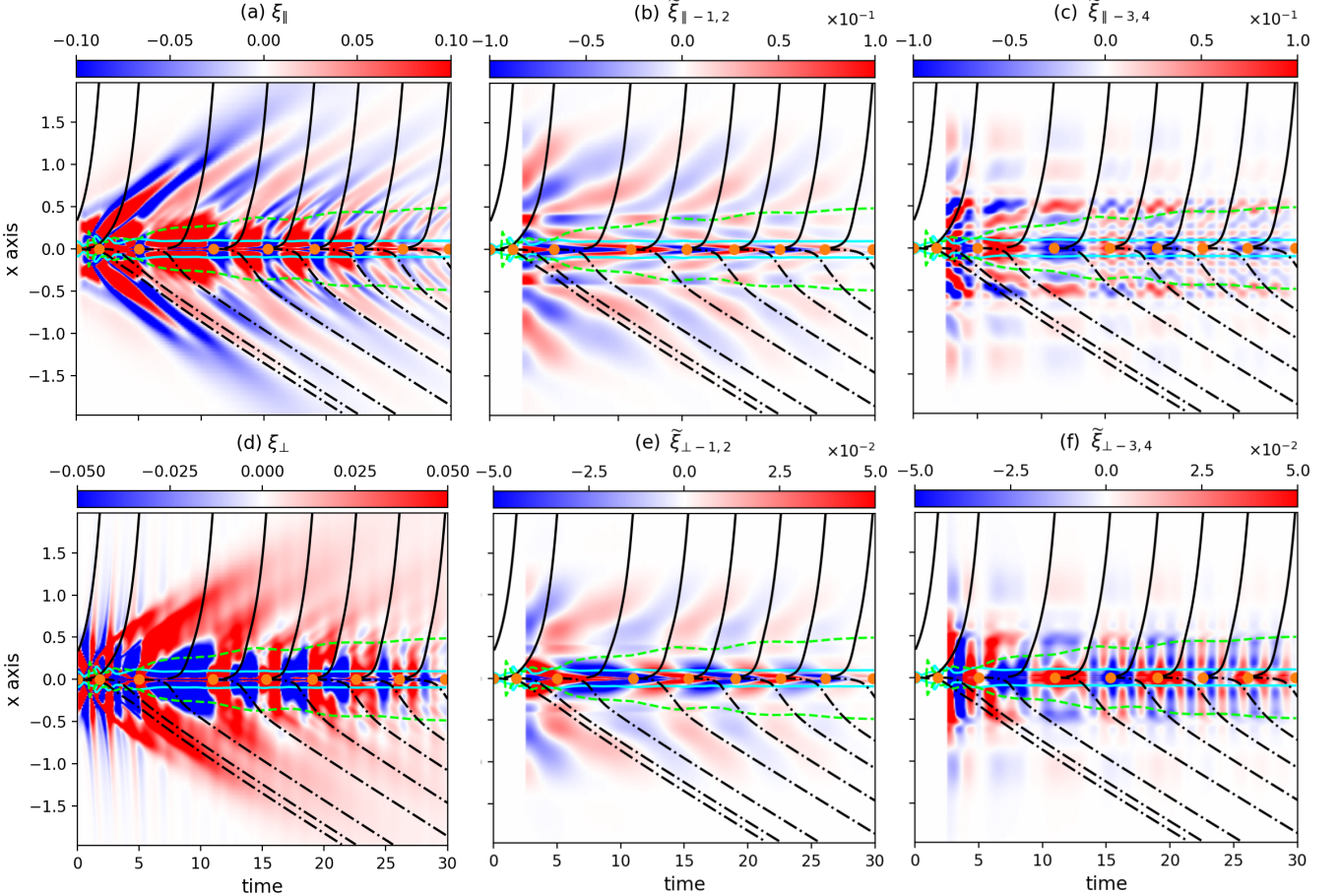


Figure 15. Time-distance diagrams for ξ_{\parallel} and ξ_{\perp} and their SPOD reconstruction along the x -axis. The orange dots mark the roots of $j_y(0,0,0,t)$, while cyan lines indicate the equipartition layer and green lines the cavity envelope. The black dashed-dotted and black continuous lines represent the slow and fast magnetoacoustic wave trajectories respectively.

both the spine and fan are deformed, with the perturbation amplitude decaying significantly after the first reconnection cycle. The maximum amplitude decrease occurs in the first OR cycle, approximately 6 times, representing a six-fold reduction (Figure 2c). Additionally, the OR perturbation continually deforms the fan plane.

This investigation utilized the approach from [Raboonik \(2021\)](#) to isolate an incompressible parallel component, ξ_A , a compressible parallel component, ξ_{\parallel} , and a compressible transverse component, ξ_{\perp} . These identifiers are not exact representations of the three fundamental MHD wave modes, but they encapsulate the essential features distinguishing wave behavior, and hence are useful in wave mode identification. This investigation also utilized Spectral Proper Orthogonal Decomposition (SPOD) to analyze the wave motions. The first four SPOD modes captured approximately 90% of the system's fluctuation energy (Figure 3). Mode 1 accounted for about 73% and was predominantly influenced by the OR period. It was found that modes 1 and 2, which together contain approximately 80% of the

fluctuation energy, were sufficient to describe the incompressible and compressible magnetoacoustic waves that share the same OR period, P . In contrast, modes 3 and 4, which account for around 10% of the fluctuation energy, were responsible for describing the waves with half the OR period ($P/2$), including compressible parallel and transverse, and incompressible waves (Figures 12 and 14).

The plasma heating generated by the reconnection jets creates a cavity in the fan plane, characterized by a region of reduced density near the null point (see Figures 9, 10a, 10d). This cavity plays a crucial role in the dynamics of the system: It traps heat, as evidenced by internal energy perturbations (see Figures 10c, 10f), and modulates wave propagation. Separately, density depletions in the equipartition layer along the spine were reported (Figure 8). This created a region of trapped waves at $z \approx \pm 0.5$ along the spine, allowing the manifestation of standing waves of period $P/2$.

Wave motions along the spine (z -axis) and fan plane (x - and y -axes) were investigated. In all three directions, common wave behavior was reported:

- (i) There exists an initial transient between $t = 0$ and $t = 10$. Compressible transverse waves (ξ_{\perp}) propagating with the fast speed and with period $P/2$ were observed along the spine as well as the fan plane along the x - and y -axes (Figures 7d, 14d and 15d).
- (ii) For each of the 3 directions, there always exists a period P wave, propagating at the local slow speed (both inside and outside the spine equipartition and fan cavity). This manifests in both ξ_{\parallel} and ξ_{\perp} , along the spine (Figures 7b and 7e), along the y -axis (Figures 14b and 14e) and along the x -axis (Figures 15b and 15e). Furthermore, Figures 13a and 13b reveal that a propagating, period P , slow wave occurs in all fan-plane directions. Figure 13c showed that period P was axisymmetric in the fan plane, with the amplitude of such slow waves stronger in the x -direction (maximum amplitude ≈ 0.5) compared to the y -direction (maximum amplitude ≈ 0.2).
- (iii) For each of the 3 directions, there always exists a second wave of period $P/2$, characterized by being trapped by density depletions along the spine (Figure 8a) and inside the fan cavity (Figures 10a and 10d). This wave manifests as a standing wave in ξ_{\parallel} and ξ_{\perp} , along the spine (Figures 7c and 7f), along the y -axis (Figures 14c and 14f) and along the x -axis (Figures 15c and 15f). Outside the density depletions along the spine and the fan cavity, different behavior is reported: a propagating fast wave with period P is observed in ξ_{\parallel} (Figures 7c, 14c and 15c), whereas wave behavior in ξ_{\perp} decays rapidly in amplitude (Figures 7f, 14f and 15f).

For the initial transient (propagating wave of period $P/2$), these are compressible transverse waves (ξ_{\perp}) propagating with the fast speed, and so we interpret these as fast magnetoacoustic waves. For the propagating wave of period P that manifests along both the spine and the whole fan plane, these are compressible waves (ξ_{\parallel}) propagating parallel to the magnetic field lines, traveling at the slow speed, and so we interpret these as slow magnetoacoustic waves.

These results also demonstrate the utility of the SPOD reconstruction: SPOD modes revealed previously-obscured wave propagation in all directions and for all three MHD waves. Note that point (ii) is derived from modes 1 and 2, which together contain approximately

80% of the fluctuation energy, and point (iii) is related to information derived from modes 3 and 4, which account for around 10% of the fluctuation energy.

Along the spine and the x -direction of the fan plane (see Figures 7 and 15), only waves that disturb the density, i.e. magnetoacoustic, were found; the incompressible wave proxy ξ_A was near zero. Incompressible waves were exclusively detected along the y -axis in the fan plane, propagating transverse to the plane containing the spine motion (Figures 11 and 12). They have period P , synchronized with the roots of $j_y(0, 0, 0, t)$, and propagate both inside and outside of the cavity at the local fast speed (Figure 12b). The local fast speed is approximately the same as the local Alfvén speed in this region, and these period P incompressible waves propagate at the local Alfvén speed. They also propagate vorticity (due to the formalism of ξ_A , Equation (9)) and thus we interpret these as a propagating Alfvén wave.

SPOD analysis also revealed low-amplitude, ξ_A standing waves with a period of $P/2$ inside the cavity. These rapidly decay outside the cavity (Figure 12c).

This work demonstrates that a 3D null point can function as a self-oscillating wave source, with its wave properties intrinsically linked to j_y oscillations at the null point. An aperiodic disturbance leads to the generation of propagating, period P , slow magnetoacoustic waves, along both the spine and the fan-plane. For a 2D X-type null point undergoing OR, Karampelas et al. (2023) has shown a direct link between the OR period P and the magnetic field strength, density and temperature (i.e. a dependence upon the local Alfvén speed and local sound speed). No such parameter study has been conducted for a 3D null. However, should the 2D results of Karampelas et al. (2023) translate to 3D, then the propagating, period P , slow magnetoacoustic waves reported in this paper open up a fascinating opportunity for indirectly deriving information about the local magnetic field strength, density and temperature, i.e. new avenues for coronal seismology.

ACKNOWLEDGMENTS

All authors acknowledge the UK Research and Innovation (UKRI) Science and Technology Facilities Council (STFC) for support from grant ST/X001008/1 and for IDL support. The research was sponsored by the DynaSun project and has thus received funding under the Horizon Europe programme of the European Union under grant agreement (no. 101131534). Views and opinions expressed are however those of the author(s) only and do not necessarily reflect those of the European Union and therefore the European Union cannot be held responsible for them. This work was also supported

by the Engineering and Physical Sciences Research Council (EP/Y037464/1) under the Horizon Europe Guarantee. This work used the Oswald High Performance Computing facility operated by Northumbria University (UK), and the DiRAC Data Intensive service (CSD3) at the University of Cambridge, managed by the University of Cambridge University Information Services on behalf of the STFC DiRAC HPC Facility (www.dirac.ac.uk). The DiRAC component of CSD3 at Cambridge was funded by BEIS, UKRI and STFC capital funding and STFC operations grants. DiRAC is part of the UKRI Digital Research Infrastructure.

Numerical simulations were conducted with LARE3D which is available at <https://github.com/Warwick-Plasma/Lare3d>. The data behind figures and the inputs from the simulation are available in Figshare at DOI:<https://doi.org/10.25398/rd.northumbria.30896033>. Additional data support the findings of this study are available from the corresponding author upon reasonable request.

Software: LARE3D (Arber et al. 2001), NumPy (Harris et al. 2020), SciPy (Virtanen et al. 2020), Matplotlib (Hunter 2007) WaLSA tools (Jafarzadeh et al. 2025).

REFERENCES

Albidah, A. B., Brevis, W., Fedun, V., et al. 2021, Phil. Trans. R. Soc. London Ser. A, 379, 20200181, doi: [10.1098/rsta.2020.0181](https://doi.org/10.1098/rsta.2020.0181)

Albidah, A. B., Fedun, V., Aldhafeeri, A. A., et al. 2022, ApJ, 927, 201, doi: [10.3847/1538-4357/ac51d9](https://doi.org/10.3847/1538-4357/ac51d9)

Arber, T. D., Longbottom, A. W., Gerrard, C. L., & Milne, A. M. 2001, Journal of Computational Physics, 171, 151, doi: [10.1006/jcph.2001.6780](https://doi.org/10.1006/jcph.2001.6780)

Benz, A. O. 2017, Living Reviews in Solar Physics, 14, 2, doi: [10.1007/s41116-016-0004-3](https://doi.org/10.1007/s41116-016-0004-3)

Browning, P. K., Gordovskyy, M., Schiavo, L. A., & Stewart, J. 2024, Fundamental Plasma Physics, 10, 100049, doi: <https://doi.org/10.1016/j.fpp.2024.100049>

Caramana, E. J., Shashkov, M. J., & Whalen, P. P. 1998, Journal of Computational Physics, 144, 70

Craig, I. J., & McClymont, A. N. 1991, Astrophysical Journal; (United States), 371, doi: [10.1086/185997](https://doi.org/10.1086/185997)

Enerhaug, E., Carlsson, M., Szydlarski, M., Gudiksen, B. V., & De Moortel, I. 2025, Astronomy & Astrophysics, 701, A137, doi: [10.1051/0004-6361/202554210](https://doi.org/10.1051/0004-6361/202554210)

Enerhaug, E., Howson, T. A., & De Moortel, I. 2024, Astronomy & Astrophysics, 681, L11, doi: [10.1051/0004-6361/202347790](https://doi.org/10.1051/0004-6361/202347790)

Goossens, M. L., Arregui, I., & Van Doorsselaere, T. 2019, Frontiers in Astronomy and Space Sciences, 6, 20, doi: [10.3389/fspas.2019.00020](https://doi.org/10.3389/fspas.2019.00020)

Harris, C. R., Millman, K. J., van der Walt, S. J., et al. 2020, Nature, 585, 357, doi: [10.1038/s41586-020-2649-2](https://doi.org/10.1038/s41586-020-2649-2)

Haynes, A. L., & Parnell, C. E. 2007, Physics of Plasmas, 14, 082107, doi: [10.1063/1.2756751](https://doi.org/10.1063/1.2756751)

Huang, Y.-M., & Bhattacharjee, A. 2016, The Astrophysical Journal, 818, 20, doi: [10.3847/0004-637X/818/1/20](https://doi.org/10.3847/0004-637X/818/1/20)

Hunter, J. D. 2007, Computing in Science & Engineering, 9, 90, doi: [10.1109/MCSE.2007.55](https://doi.org/10.1109/MCSE.2007.55)

Jafarzadeh, S., Jess, D. B., Stangalini, M., et al. 2025, Nature Reviews Methods Primers, 5, 21, doi: [10.1038/s43586-025-00392-0](https://doi.org/10.1038/s43586-025-00392-0)

Karampelas, K., McLaughlin, J. A., J. Botha, G. J. J., & Régnier, S. 2023, The Astrophysical Journal, 943, 131, doi: [10.3847/1538-4357/acac90](https://doi.org/10.3847/1538-4357/acac90)

Kumar, P., Nakariakov, V. M., Karpen, J. T., & Cho, K.-S. 2024, Nature Communications, 15, 2667, doi: [10.1038/s41467-024-46736-4](https://doi.org/10.1038/s41467-024-46736-4)

Lumley, J. L. 1967, in Atmospheric Turbulence and Wave Propagation (Moscow: Nauka), 166

McLaughlin, J. A., De Moortel, I. and Hood, A. W., & Brady, C. S. 2009, A&A, 493, 227, doi: [10.1051/0004-6361:200810465](https://doi.org/10.1051/0004-6361:200810465)

McLaughlin, J. A., & Hood, A. W. 2006, Astronomy & Astrophysics, 459, 641, doi: [10.1051/0004-6361:20065558](https://doi.org/10.1051/0004-6361:20065558)

McLaughlin, J. A., Hood, A. W., & De Moortel, I. 2011, Space Science Reviews, 158, 205, doi: [10.1007/s11214-010-9654-y](https://doi.org/10.1007/s11214-010-9654-y)

McLaughlin, J. A., Thurgood, J., & MacTaggart, D. 2012, Astronomy and Astrophysics, doi: [10.1051/0004-6361/201220234](https://doi.org/10.1051/0004-6361/201220234)

Mondal, S., Srivastava, A. K., Pontin, D. I., et al. 2024, The Astrophysical Journal, 977, 235, doi: [10.3847/1538-4357/ad9022](https://doi.org/10.3847/1538-4357/ad9022)

Nakariakov, V. M., Foullon, C., Verwichte, E., & Young, N. P. 2006, Astronomy & Astrophysics, 452, 343, doi: [10.1051/0004-6361:20054608](https://doi.org/10.1051/0004-6361:20054608)

Parnell, C. E., Smith, J. M., Neukirch, T., & Priest, E. R. 1996, Physics of Plasmas, 3, 759, doi: [10.1063/1.871810](https://doi.org/10.1063/1.871810)

Pontin, D. I., & Priest, E. R. 2022, Living Reviews in Solar Physics, 19, 1, doi: [10.1007/s41116-022-00032-9](https://doi.org/10.1007/s41116-022-00032-9)

Priest, E. R., Hornig, G., & Pontin, D. I. 2003, Journal of Geophysical Research: Space Physics, 108, 2002JA009812, doi: [10.1029/2002JA009812](https://doi.org/10.1029/2002JA009812)

Priest, E. R., & Pontin, D. I. 2009, Physics of Plasmas, 16, 122101, doi: [10.1063/1.3257901](https://doi.org/10.1063/1.3257901)

Raboonik, A. 2021, PhD thesis, doi: [10.26180/19233735.v1](https://doi.org/10.26180/19233735.v1)

Raboonik, A., Tarr, L. A., & Pontin, D. I. 2024, The Astrophysical Journal, 967, 80, doi: [10.3847/1538-4357/ad3bb6](https://doi.org/10.3847/1538-4357/ad3bb6)

Régnier, S., Parnell, C. E., & Haynes, A. L. 2008, Astronomy & Astrophysics, 484, L47, doi: [10.1051/0004-6361:200809826](https://doi.org/10.1051/0004-6361:200809826)

Sabri, S., Ebadi, H., & Poedts, S. 2021, The Astrophysical Journal, 922, 123, doi: [10.3847/1538-4357/ac242d](https://doi.org/10.3847/1538-4357/ac242d)

—. 2022, The Astrophysical Journal, 924, 126, doi: [10.3847/1538-4357/ac3b5f](https://doi.org/10.3847/1538-4357/ac3b5f)

Schiavo, L. A. C. A., Botha, G. J. J., & McLaughlin, J. A. 2025, The Astrophysical Journal, 993, 239, doi: [10.3847/1538-4357/ae09ad](https://doi.org/10.3847/1538-4357/ae09ad)

Shibata, K., Nakamura, T., Matsumoto, T., et al. 2007, Science, doi: [10.1126/science.1146708](https://doi.org/10.1126/science.1146708)

Sieber, M., Paschereit, C. O., & Oberleithner, K. 2016, Journal of Fluid Mechanics, 792, 798–828, doi: [10.1017/jfm.2016.103](https://doi.org/10.1017/jfm.2016.103)

Sirovich, L. 1987, Quarterly of Applied Mathematics, 45, 561

Taira, K., Brunton, S. L., Dawson, S. T. M., et al. 2017, AIAA Journal, 55, 4013, doi: [10.2514/1.J056060](https://doi.org/10.2514/1.J056060)

Tarr, L. A., Linton, M., & Leake, J. 2017, The Astrophysical Journal, 837, 94, doi: [10.3847/1538-4357/aa5e4e](https://doi.org/10.3847/1538-4357/aa5e4e)

Thurgood, J., Pontin, D. I., & McLaughlin, J. A. 2017, The Astrophysical Journal, doi: [10.3847/1538-4357/aa79fa](https://doi.org/10.3847/1538-4357/aa79fa)

Virtanen, P., Gommers, R., Oliphant, T. E., et al. 2020, Nature Methods, 17, 261, doi: [10.1038/s41592-019-0686-2](https://doi.org/10.1038/s41592-019-0686-2)

Webb, D. F., & Howard, T. A. 2012, Living Reviews in Solar Physics, 9, 3, doi: [10.12942/lrsp-2012-3](https://doi.org/10.12942/lrsp-2012-3)

Wyper, P., & Jain, R. 2010, Physics of Plasmas, 17, 092902, doi: [10.1063/1.3480639](https://doi.org/10.1063/1.3480639)

Wyper, P. F., & Jain, R. 2011, Journal of Plasma Physics, 77, 843, doi: [10.1017/S0022377811000262](https://doi.org/10.1017/S0022377811000262)

Wyper, P. F., & Pontin, D. I. 2014, Physics of Plasmas, 21, 102102, doi: [10.1063/1.4896060](https://doi.org/10.1063/1.4896060)